ADVANCED FUNCTIONAL MATERIALS
www.afm-journal.de

Single-Source Vapor-Deposition of $MA_{1-x}FA_xPbI_3$ Perovskite Absorbers for Solar Cells

Tatiana Soto-Montero, Suzana Kralj, Wiria Soltanpoor, Junia S. Solomon, Jennifer S. Gómez, Kassio P. S. Zanoni, Abhyuday Paliwal, Henk J. Bolink, Christoph Baeumer, Arno P. M. Kentgens, and Monica Morales-Masis**

Vapor deposition of halide perovskites presents high potential for scalability and industrial processing of perovskite solar cells. It prevents the use of toxic solvents, allows thickness control, and yields conformal and uniform coating over large areas. However, the distinct volatility of the perovskite organic and inorganic components currently requires the use of multiple thermal sources or two-step deposition to achieve the perovskite phase. In this work, single-source, single-step $MA_{1-x}FA_xPbI_3$ thin film deposition with tunable stoichiometry by pulsed laser deposition is demostrated. By controlling the laser ablation of a solid target containing adjustable MAI:FAI:PbI_2 ratios, the room temperature formation of cubic α-phase $MA_{1-x}FA_xPbI_3$ thin films is demonstrated. The target-to-film transfer of the ablated species, including the integrity of the organic molecules and the desired MA^+:FA^+ ratio, is confirmed by x-ray photoelectron spectroscopy and solid-state NMR. Photoluminescence analysis further confirms the shift of the bandgap with varying the MA^+:FA^+ ratio. Finally, proof-of-concept n-i-p solar cells with 14% efficiency are demonstrated with as-deposited non-passivated pulsed laser deposition (PLD)-$MA_{1-x}FA_xPbI_3$. This study opens the path for future developments in industry-compatible vapor-deposition methods for perovskite solar cells.

1. Introduction

Thin-film emerging photovoltaic technologies such as perovskite solar cells are one of the most attractive options for top cell integration in monolithic perovskite/silicon tandem solar cells.[1] For this, fabrication methods that fulfill next-generation photovoltaic requirements, for instance, conformal deposition on textured surfaces and thickness control, are of utmost importance. Further, control over film stoichiometry and structural polymorphs of complex perovskite compositions by employing reproducible and scalable processes is highly desired. Some approaches to comply with the previous requirements utilize hybrid vapor-solution or co-evaporation methods for depositing the top hybrid halide perovskite absorber.[2,3] The advantages of vapor-based over solution-based methods include most of the previously mentioned requirements and the viability of heterostructures while avoiding toxic solvents.[4] Co-evaporation has been successfully applied to fabricate large-area single-junction devices containing methylammonium lead iodide ($MAPbI_3$) as an absorber layer with power conversion efficiencies (PCE) exceeding 18% in minimodules (21 cm^2 active area).[5] However, complex compositions as needed for wide-bandgap[6–9] halide perovskites or to enhance the structural or thermal stability of the materials require an increasing number of thermal evaporation sources (> 2), resulting in challenges to control film stoichiometry.[10] Regarding structural stability, the incorporation of MA^+ into $FAPbI_3$ has been demonstrated to stabilize the cubic α-phase of $MA_{1-x}FA_xPbI_3$ perovskites due to the smaller ionic radius of the MA^+ cation (2.70 Å) compared to the FA^+ cation (2.79 Å); i.e., reducing the octahedral strain that causes the transition of $FAPbI_3$ from the cubic α-phase to a non-perovskite yellow δ-phase.[11,12] The vast majority of approaches to grow $MA_{1-x}FA_xPbI_3$ perovskites have been solution-based methods,[13,14] but vacuum-based methods have also been reported. Co-evaporation of $MA_{1-x}FA_xPbI_3$ was demonstrated,[15] showing promising single junctions with PCEs up to 18.8% and later on incorporated on tandems reaching a PCE of 24.6%.[2] Yet, as mentioned above, thin film formation with this double A-site cation composition requires three independent

T. Soto-Montero, S. Kralj, W. Soltanpoor, J. S. Solomon, C. Baeumer, M. Morales-Masis
MESA+ Institute for Nanotechnology
University of Twente
Enschede 7500 AE, The Netherlands
E-mail: t.d.s.sotomontero@utwente.nl; m.moralesmasis@utwente.nl
J. S. Gómez, A. P. M. Kentgens
Institute for Molecules and Materials
Radboud University
Nijmegen 6525 AJ, The Netherlands
K. P. S. Zanoni, A. Paliwal, H. J. Bolink
Instituto de Ciencia Molecular
Universidad de Valencia
C/Catedrático J. Beltrán 2, Paterna 46980, Spain
The ORCID identification number(s) for the author(s) of this article can be found under https://doi.org/10.1002/adfm.202300588.

DOI: 10.1002/adfm.202300588

thermal evaporation sources, which could pose a challenge for scalability and stoichiometry control.

Regarding pulsed laser deposition (PLD), single-source vapor deposition of halide perovskite films has been reported for $CsSnI_3$,[16] $CsPbBr_3$,[17] double perovskite $Cs_2AgBiBr_6$,[18] and $MAPbI_3$ films on flat substrates and textured silicon wafers.[19,20] Previous studies on PLD-based perovskite absorbers reported solar cell efficiencies of 10.9% for $MAPbI_3$[20] (and later of 12.2% by RIR-MAPLE[21]), 7.66% for $MAPb(I_xCl_{x-1})_3$,[22] and 6.3% for $CsPbBr_3$.[17]

In this work, we demonstrate PLD of halide perovskites containing both, MA^+ $(NH_3\text{-}CH_3)^+$ and FA^+ $((NH_2)_2\text{-}CH)^+$ organic cations, resulting in the formation of $MA_{1-x}FA_xPbI_3$ (x = 0.22–0.55) perovskite films with tunable stoichiometry from a single dry source. The first steps toward scalability of the method are furthermore demonstrated by investigating the formation and composition of the films grown by scanning the substrate during PLD deposition. The proof-of-concept solar cells showed an improved PCE of up to 14% without any passivation or contact optimization. The benefits of PLD as an all-dry process[23–25] and the possibility of wafer-scale depositions and conformal growth of thin films over textured surfaces make PLD an appealing method for further device optimization and future incorporation in, e.g., tandem solar cells.[26,27]

2. Results and Discussion

2.1. Stoichiometry Control of Thin Films by PLD

The PLD process is carried out in a vacuum system in which the deposition pressure is controlled by introducing an inert gas.[28] **Figure 1**a illustrates the PLD process, where a pulsed UV laser (248 nm) is used as a direct energy source that ablates

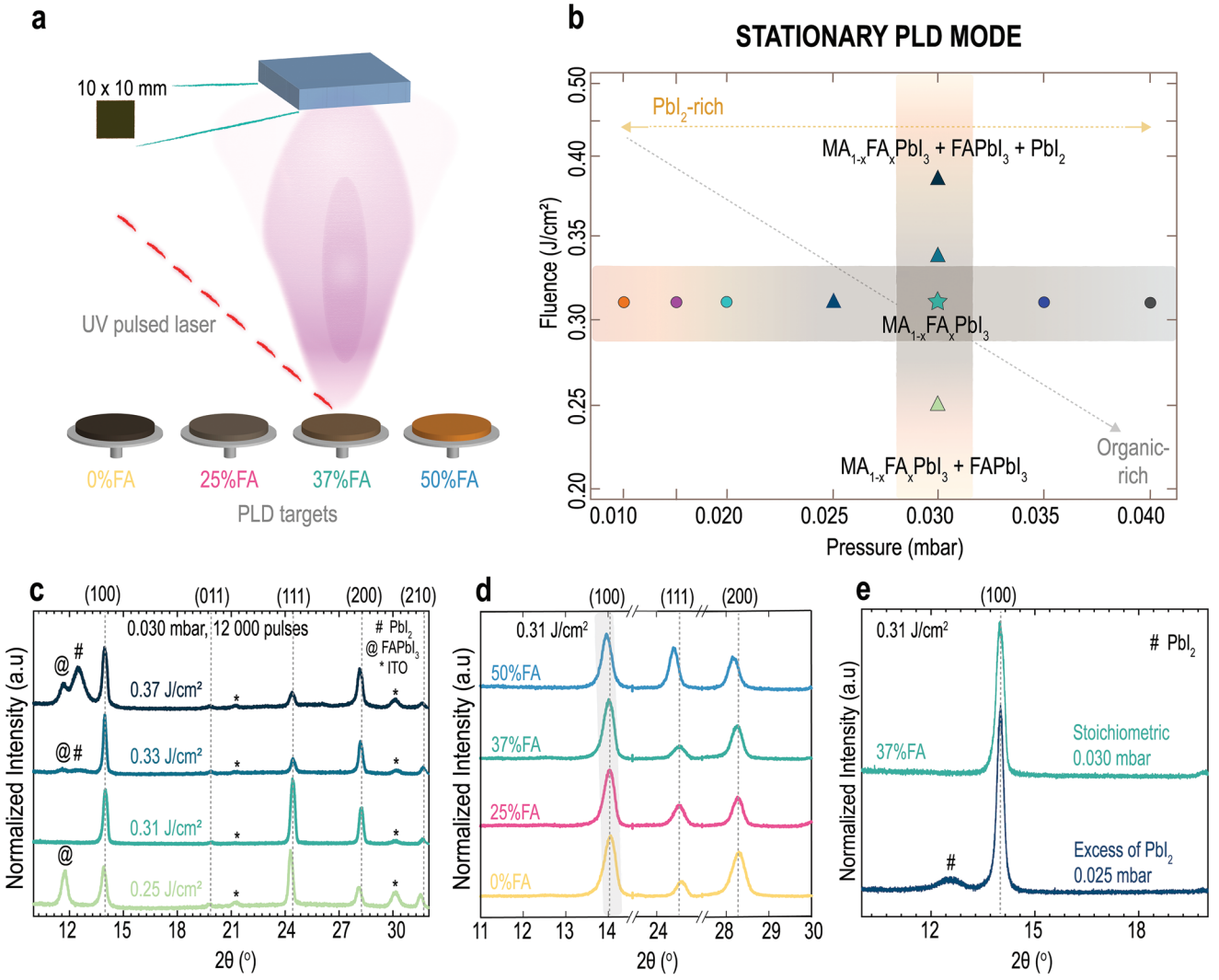

Figure 1. a) Schematics of the PLD process in the stationary mode. b) Dependence of the $MA_{1-x}FA_xPbI_3$ film phases on the deposition pressure and laser fluence during stationary PLD. c) XRD patterns of films grown using different laser fluences at a constant pressure of 0.030 mbar from a 37% FA^+ target, d) thin films grown at the optimized fluence of 0.31 J cm^{-2} from targets containing different FA^+ ratios (from 0 to 50%) and e) influence of the deposition pressure on the formation of PbI_2 rich phases as indicated by XRD (film grown from a FA^+ = 37% target).

a small volume of the target containing the material of interest, which is transferred in a confined (forward-directed) plasma plume (material flux) towards the substrate for evaporative film growth. The inert gas promotes the thermalization of the species ablated from the target at high-process pressure regimes ($> 10^{-3}$ mbar).[26] This deposition pressure also plays a crucial role in the element distribution in the plasma plume and in the final film morphology.[19] For hybrid halide perovskites film growth, the inert gas used is argon (Ar).

The choice of the laser energy density (or fluence) is related to the PLD target composition. The laser energies are chosen to reach an ablation threshold that results in ablation independent of the vapor pressures of the target constituents.[29] The target quality also impacts film growth, stoichiometry, and particulate density. In general, the phase of the targets does not need to be the same as that of the desired film but should be highly dense to guarantee uniform ablation.[22] Here we employ an all-dry mechanochemical synthesis approach to prepare hybrid halide perovskite PLD targets as previously reported (Experimental Section and Figures S1 and S2, Supporting Information).[19,16] The latter enables us to change the target composition, e.g., cation ratio, based on the desired thin-film stoichiometry under specific PLD deposition parameters.

From the lessons learned regarding the growth of the archetypical hybrid halide perovskite $MAPbI_3$ by PLD,[19] in this study, we employed targets with an excess of 8:1 organics: inorganics $(MA_{1-x}FA_x)I:PbI_2$ (x = 0.12–0.50) to compensate for the dissimilar atomic masses and volatilities of the target constituents (metal halide and organohalides). Moreover, to keep the integrity of the organic molecules, a low fluence regime is preferred. To find the optimal growth conditions that allow reproducible growth of $MA_{1-x}FA_xPbI_3$ thin films, we investigate a fluence range going from 0.2 up to 0.6 J cm^{-2} and deposition pressures from 0.01 up to 0.05 mbar.

2.1.1. Stationary PLD Mode

To study the transfer of elements from target to film, we first performed PLD in stationary mode, i.e., with the target and substrate facing each other constantly during the film formation. Figure 1b presents the relation between fluence and deposition pressure on the different film phases experimentally obtained (see also Figure S2, Supporting Information for the individual XRD patterns measured). The graph shows that there is a specific parameter window for growing $MA_{1-x}FA_xPbI_3$ perovskites at RT where the photoactive cubic α-phase can be stabilized. We found that films grown at pressures ≥ 0.035 mbar tend to be porous, with excess organics or amorphous (no diffraction peaks detected), while films grown at pressures in the range of 0.025 and 0.035 mbar are dense, but the pure perovskite phase formation depends on the fluence. Here 0.31 J cm^{-2} laser fluence leads to pure $MA_{1-x}FA_xPbI_3$ perovskite films, as will be discussed in the following sessions. Films grown at even lower pressures (≤ 0.02 mbar) or higher fluences (> 0.4 J cm^{-2}) tend to be PbI_2-rich or amorphous, depending on the laser energy. In the case of hybrid halide perovskites, these low-pressure regimes promote the scattering of lighter elements; thus, fewer organic species landing on the substrate.

Figure 1c shows the XRD patterns of films grown employing different laser fluences for a constant pressure of 0.03 mbar. Films grown at 0.37 J cm^{-2}, present an excess of PbI_2 and the non-perovskite δ-phase of $FAPbI_3$, as seen from the diffraction peak at 2θ = 12.6° and 11.7°, respectively. On the other hand, films grown at 0.25 J cm^{-2} showed no presence of PbI_2 but δ-$FAPbI_3$. The indication of PbI_2 excess observed for the films grown with a fluence above 0.31 J cm^{-2} could be related to partial decomposition of the organic components when increasing fluence or to changes in the composition (e.g., elemental distribution) of the plasma plume. To draw a conclusion on this, dedicated experiments of in situ plasma monitoring would be required.[29] We found that when growing films using 0.31 J cm^{-2}, no visible PbI_2 or δ-$FAPbI_3$ peaks appear in the XRD patterns, and only the diffraction peaks corresponding to the cubic $MA_{1-x}FA_xPbI_3$ phase are observed. This suggests near-stoichiometric transfer from target to film, as confirmed by XPS and NMR (vide infra).

Knowing the deposition parameters (pressure and fluence) that could lead to the near stoichiometric transfer, the next step focused on demonstrating the control of the MA^+: FA^+ cation ratio in the films. Taking into account previous studies of bulk perovskites,[30,31] physical vapor methods,[2,15] and solution processes[32,33] that have shown the critical role of the MA^+: FA^+ ratio on the stabilization of the cubic phase and optimum optoelectronic properties, we dedicated our study on FA^+ molar content between 25–50%. Consequently, we prepared and tested three PLD targets with the compositional ratio of $(MA_{1-x}FA_x)I$: PbI_2 = 8:1 where x = 0.25, 0.37, 0.50, representing the 25, 37, and 50% FA^+ molar content in the targets. Figure 1d displays the XRD patterns of highly oriented (100) and (111) $MA_{1-x}FA_xPbI_3$ films grown on glass/ITO/SnO_2/PCBM substrates. For comparison, a film from a $MAPbI_3$ target (0% FA) is presented to distinguish the shift of the main XRD peaks at ≈14°, ≈24.5°, and ≈28° toward lower 2θ correlated to the incorporation of the bigger FA^+ cation into the lattice. Consequently, lattice parameter values of 6.307, 6.321, and 6.339 Å were obtained from films grown from the PLD targets with 25, 37, and 50% FA^+ molar content, respectively (Table S1, Supporting Information). We also tested PLD targets containing 75% and 100% FA^+ (Figure S4, Supporting Information). Films containing ≥ 75% FA^+ molar content showed the coexistence of the $MA_{1-x}FA_xPbI_3$ cubic α-phase and the non-perovskite δ-phase of $FAPbI_3$.

For the optimized composition of 37% FA^+ molar content in the target, we demonstrate the possibility of having a slight excess of PbI_2 (2θ = 12.6°) while avoiding the presence of the δ-phase (2θ = 11.7°) through modest changes in the deposition pressure as shown in Figure 1d. As previously reported, a slight excess of PbI_2 could be beneficial for the performance of solar cells.[34–36]

2.1.2. Scanning PLD Mode: Increasing the PLD Coating Area

Raster scanning of the substrate over the ablation plume can produce uniform films over larger areas.[26,37] After understanding the fluence-pressure relationships to grow $MA_{1-x}FA_xPbI_3$ perovskites in stationary mode, we investigated the coverage, structural, and stoichiometric changes of the film

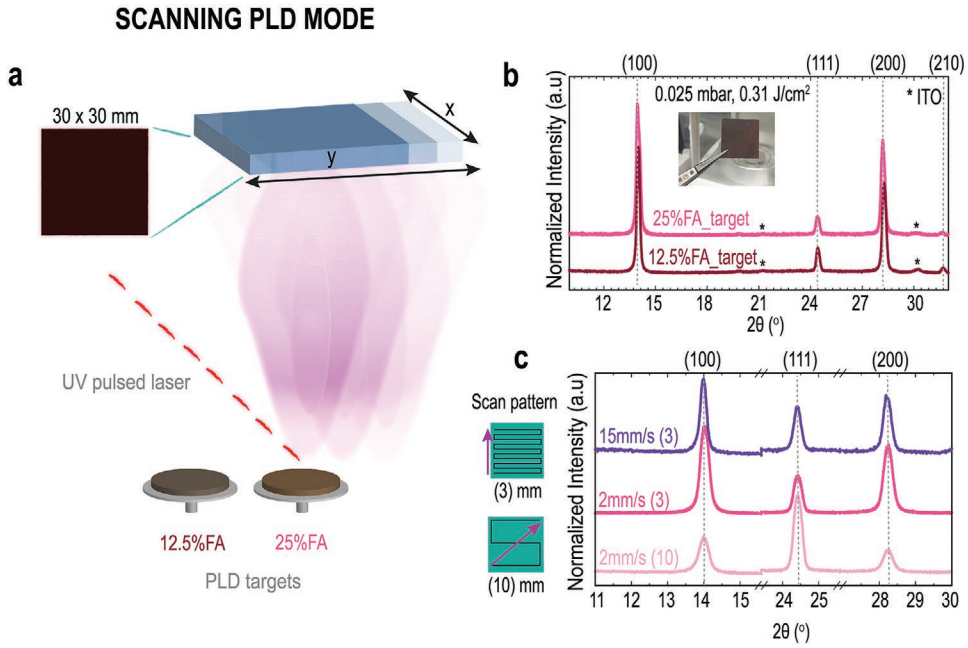

Figure 2. a) Schematics of the PLD process in the scanning mode, i.e., substrate scanning in the horizontal plane above the ablated plume to increase the PLD coated area: b) XRD patterns of films grown from targets with two different MA^+/FA^+ ratios (12.5% and 25% FA^+) and, c) XRD patterns of films grown with different scanning speed or step width, showing its impact on the growth orientation of the $MA_{1-x}FA_xPbI_3$ films.

growth when the substrate is scanned in the *x*- and *y*-directions following a raster pattern (**Figure 2**a,c). We tested a scan area of 30×30 mm^2 to match typical lab-based solar cell substrates.

Films grown at 0.030 mbar showed small diffraction signals at $2\theta = 10°$, indicating the presence of a slight organic excess contrary to the films grown employing the stationary mode (Figure S5, Supporting Information). As the organic species are lighter than the PbI_2, one may hypothesize that the edges of the ablated plume are organic-rich.[29] During scanning, the substrate has a higher exposure to these regions of the plume as compared to the stationary case, therefore suggesting the reason for the slight organic excess. This was confirmed with an additional experiment where a pure PbI_2 thin film was left exposed to the edges of the plasma plume, as will be described in Section 2.3 and Figure S17 (Supporting Information). To avoid this organic excess, the deposition pressure was further reduced to 0.025 mbar.

Films grown at 0.025 mbar deposition pressure display the formation of $MA_{1-x}FA_xPbI_3$ perovskite films with the textured and stoichiometric cubic α-phase (see Figure 2b). Based on the findings with the stationary PLD mode, lowering the pressure led to slightly higher PbI_2 incorporation, compensating for the excess organic due to scanning. The cation ratio MA^+: FA^+ is also being modified by the scanning deposition, resulting in more FA^+ molecules adhering onto the film, as confirmed by X-ray photoelectron spectroscopy (XPS) (Section 2.2) and XRD (Table S1, Supporting Information). From this, we conclude that the cation ratio needed in the target for the scanning versus stationary mode should be optimized independently to control the desired film stoichiometry.

Finally, Figure 2c reveals the role of the step width when scanning the substrate. Step widths ≥ 6 mm modified the preferential (100) orientation of the thin films toward (111) orientation. On the other hand, keeping the step width at 3 mm and adjusting the speed does not seem to alter the structure of the films. Note that the step width will also affect the thickness uniformity along the substrate, therefore being an important subject of study for upscaling to wafer-size areas. Here we ensured that the 3 mm step width delivers uniform thickness across the 30×30 mm^2 area.

In summary, when employing the stationary mode, near-stoichiometric transfer of the target components can be achieved; however, because of the directional nature of the PLD plasma plume, only a small area of 10×10 mm^2 of homogeneous thickness and composition can be obtained. On the other hand, the scanning mode allows increasing the deposition area, here demonstrated on a 30×30 mm^2 area, due to the movement of the substrates in the *x*- and *y*-direction following a raster pattern in front of the plasma plume. This dynamic deposition will be more sensitive to possible elemental distribution in the plasma, e.g., higher organic content at the plasma edges, resulting in films with richer organic content as compared to films deposited in the stationary PLD mode. This is overcome by independently tuning the targets' composition specifically for the static and scanning mode. While we demonstrated the scanning mode on a 30×30 mm^2 areas, this approach can be extended to wafer-scale as demonstrated previously for transparent conducting oxides.[26,38]

From this study, we selected the best deposition parameters to achieve pure phase $MA_{1-x}FA_xPbI_3$ thin films for the static and scanning PLD modes, being a fluence of 0.31 J cm^{-2} and a pressure of 0.030 and 0.025 mbar, respectively. All films characterized are ≈500 nm thick. These are the reference parameters used for the rest of the analysis and solar cell fabrication.

2.2. Thin-Film Compositional and Optoelectronic Analysis

XPS measurements were performed to study the surface chemical environment of the PLD $MA_{1-x}FA_xPbI_3$ films.[39–42] Survey spectra were measured for each sample (Figure S6, Supporting Information), revealing the presence of lead (Pb), iodine (I), carbon (C), and nitrogen (N). The presence of oxygen (O_2) is due to the brief air exposure (< 1 min) of the films during the transfer from the glovebox to the XPS. We focused on the main chemical states corresponding to the $MA_{1-x}FA_xPbI_3$ perovskites, i.e., Pb—I and N—C species from the MA^+ ($\mathbf{N}H_3$-CH_3)$^+$ and FA^+ (($\mathbf{N}H_2$)$_2$-CH)$^+$ cations. **Figure 3**a displays the high-resolution spectrum of N 1s, Pb 4f, and I 3d species. Both the Pb and I spectra were fitted in two contributions due to the spin-orbit splitting centered at 138.2 ± 0.2; 143.1 ± 0.2 eV, and 618.9 ± 0.1; 630.4 ± 0.1 eV, respectively. These signals are attributed to the lead bonding with iodine, Pb—I, ascribed to the presence of $[PbI_6]^{4-}$ in the octahedron units of the perovskite frame.[41] No peak at ≈136.5 eV corresponding to metallic lead Pb^0 was found, suggesting no degradation.[40,43]

Moreover, the spectra exhibit symmetrical peaks of similar width for all films, indicating a homogeneous surface composition (Table S3, Supporting Information). Similarly, the N 1s spectrum was decomposed into two chemical species at 400.4 ± 0.1 and 402.1 ± 0.1 eV assigned to MA^+ ($\mathbf{N}H_3$-CH_3)$^+$ and FA^+ (($\mathbf{N}H_2$)$_2$-CH)$^+$ cations, respectively.[41,45,46] The chemical environment difference of the organic cations clearly identifies the individual binding energy components, while the intensity variations are attributed to the different cation ratios MA^+: FA^+ within the studied films. To correlate the cation ratio of the different thin films, we prepared and measured reference stoichiometric targets (1.5 mm thick) of $MAPbI_3$, $FAPbI_3$, $MA_{0.75}FA_{0.25}PbI_3$, and $MA_{0.50}FA_{0.50}PbI_3$ (Figure S6, Supporting Information). We found that films deposited with the stationary mode show a MA^+: FA^+ ratio close to that of the PLD target, which agrees with the 2θ shift and the lattice parameter values obtained by XRD. Films deposited employing the scanning mode present a higher content of FA^+ compared to the molar percentage of the PLD target. That is why modifying the PLD target cation ratio is crucial to achieving stoichiometry control of thin films during the scanning mode deposition. Also, the C 1s signals display three distinguishable chemical species that were decomposed into C-(C, H) at 284.85 eV attributed to adventitious carbon and two carbon bonded to nitrogen signals at 286.2 ± 0.2 and 287.9 ± 0.1 eV associated with the presence of ($\mathbf{N}H_3$-CH_3)$^+$ (MA^+) and (($\mathbf{N}H_2$)$_2$-CH)$^+$, respectively (Figure S7, Supporting Information).[34] The C 1s signals were analyzed qualitatively but not considered for further analysis due to their complexity, as suggested for the case of hybrid halide perovskites in literature.[39,40] Other possible peaks corresponding to dissociation or degradation of the organic molecules, such as CH_3I (285.3 eV) and CH_3-NH_2 (285.4 eV), were not identified during the fitting; however, their absence is challenging to confirm due to the overlapping with other peaks at similar binding energies.[43]

Table S2 (Supporting Information) summarizes peak energy values and other characteristics of the main core levels of the studied $MA_{1-x}FA_xPbI_3$ films. It has been shown previously that the Pb, I, and N peak position of the halide perovskites vary from one deposition technique to another and for different halide perovskite compositions, which could be one reason for the small chemical shifts observed for the Pb 4f peak family.[40,45] Further, changes in the quality of the contact layer (SnO_2 np/PCBM) and reactions taking place at the contact/perovskite interface could alter the final results.[47] Besides, the well-defined peaks of the N1s core levels give insights into the integrity of the organic molecules in the film.

Even though XPS could be employed for quantitative analysis or correlation of cation ratios, it is a surface-sensitive technique focused on the first few nanometers of a thin film. For bulk compositional analysis, solid-state NMR is a powerful technique that provides insights about the local environment of nuclei in a structure, for instance, proton ^1H and carbon ^{13}C, which are nuclei present in the organic molecules. These local environments are represented in different signals in the spectrum that can be employed to quantify the cation ratios accurately.[48–50] Moreover, NMR techniques present an advantage over XRD techniques due to the ability to distinguish molecules in amorphous phases. The quantification of organic cations employing liquid NMR has been reported.[2,51] However, the quantification of solid-state NMR spectra can be more demanding either due to resolution issues or because of the polarization transfer steps used. Therefore, in this study, we implemented fast magic angle spinning (MAS) solid-state ^1H NMR, which leads to significantly improved spectral resolution and allows for quantitation using straightforward single pulse excitation. Although acquiring NMR spectra of bulk perovskite is straightforward, a mass-limited sample is a drawback when studying thin films because of the need to scrape several thin films to get enough sample amount to fill in the rotor.[52] As a result, we carried out the ^1H NMR analysis on thin films prepared in the stationary mode from a representative target containing 37% of FA^+. Figure 3b displays the ^1H NMR spectra of $MA_{1-x}FA_xPbI_3$ films with well-resolved peaks corresponding to the $\mathbf{CH}3$-NH_3 (MA_{CH3}, 3.49 ppm), CH_3-$\mathbf{NH}3$ (MA_{NH3}, 6.36 ppm), $\mathbf{NH}2$-CH-$\mathbf{NH}2$ (FA_{NH2}, 7.50 ppm), and NH_2-$\mathbf{CH}$-NH_2 (FA_{CH}, 8.26 ppm) which are in agreement with the signals reported in the literature.[30,31,53] However, extra peaks at 6.79 ppm, 7.85 ppm, 8.04 ppm, and 8.56 ppm were also identified, which could correspond to amorphous organic fractions, within the film.[52,54,55] Unfortunately the low sample amount prohibits ^{13}C NMR analysis of the films which would be valuable to identify the origin.[56,57]

Consequently, ^1H relaxation time experiments T_1 showed no indication of phase segregation but shorter values than expected when compared to bulk perovskites (in Table S4, Supporting Information).[58] Yet, more experiments must be done to clarify the extra signal observed and the difference in the T_1 experiments. Peak integration was employed to quantify the individual components. We find a cation ratio of 66: 34 MA^+: FA^+, nearly similar to the XPS cation ratio 63: 37 MA^+:FA^+, which confirms the near stoichiometric transfer of two distinct organic cations (MA^+ and FA^+) from a single source by PLD with stationary mode.

Regarding the optical properties of the films and their correlation with composition, **Figure 4**a shows the redshift in the PL peak position with increasing the content of FA^+ on the films grown with the PLD stationary mode. The PL peak position is

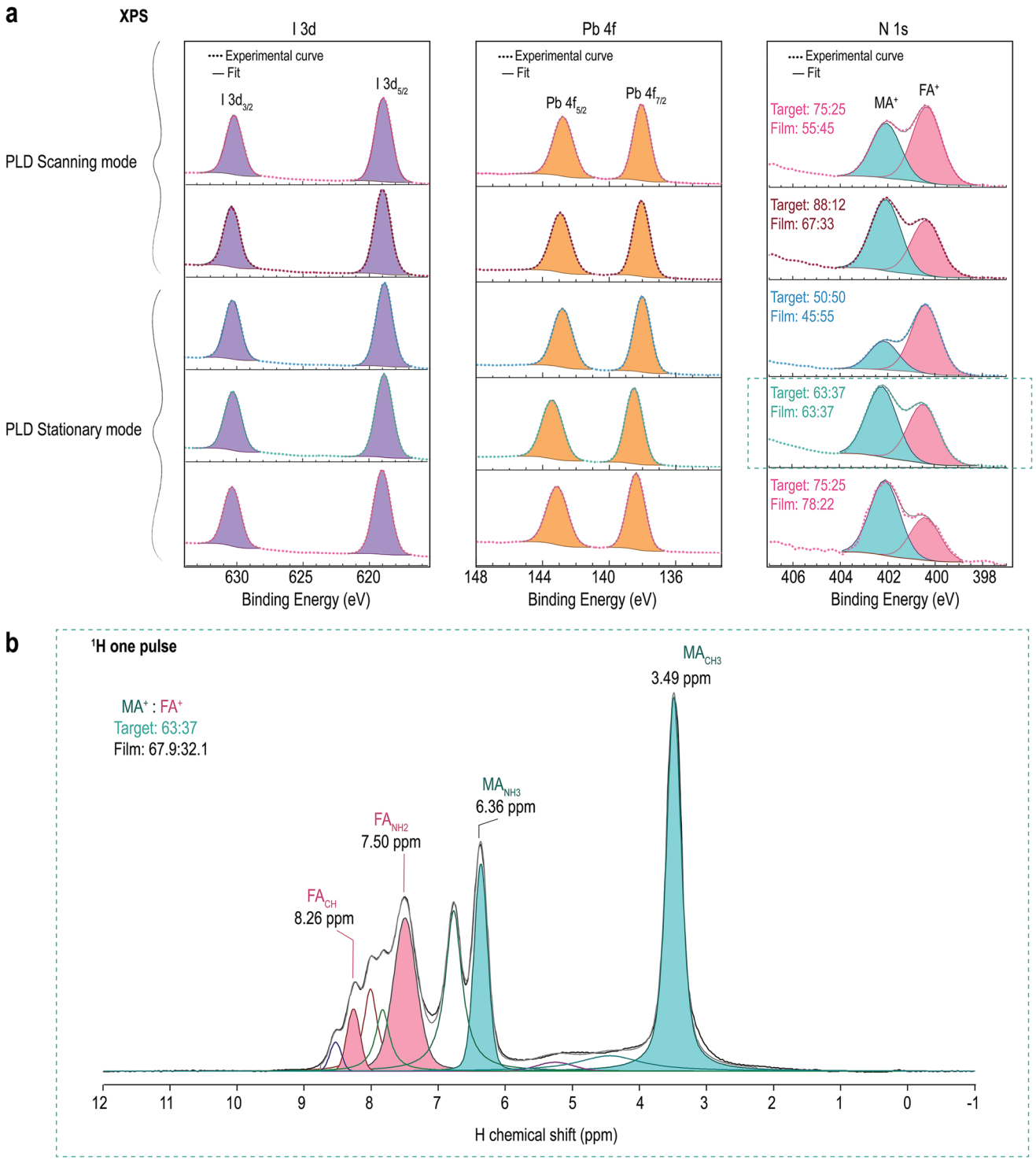

Figure 3. a) N 1s, Pb 4f, and I 3d core levels spectra of $MA_{1-x}FA_xPbI_3$ thin films grown from PLD targets with a FA^+ molar content between 12.5–50% employing the stationary and scanning PLD modes.[44] b) ^1H one pulse spectrum of $MA_{1-x}FA_xPbI_3$ thin films from target 37% FA^+ in stationary mode recorded at $B_0 = 22.3$ T with $\nu_R = 40$ kHz for the quantification of the cation ratio MA^+: FA^+ on the thin-film bulk.

centered at 1.61 eV for 0% FA^+ and moves up to 1.57 eV for 50% FA^+, all in accordance with the literature.[59] Figure 4b presents the comparison of the measured PL spectra for the films containing 25% FA^+ (top) and 50% FA^+ (bottom), grown with the stationary and scanning PLD mode. The PL reference, consisting of a powder sample ($MA_{1-x}FA_xPbI_3$ with $x = 25$ and 50) prepared via mechanosynthesis of the stoichiometric components, shows good agreement between films and stoichiometric

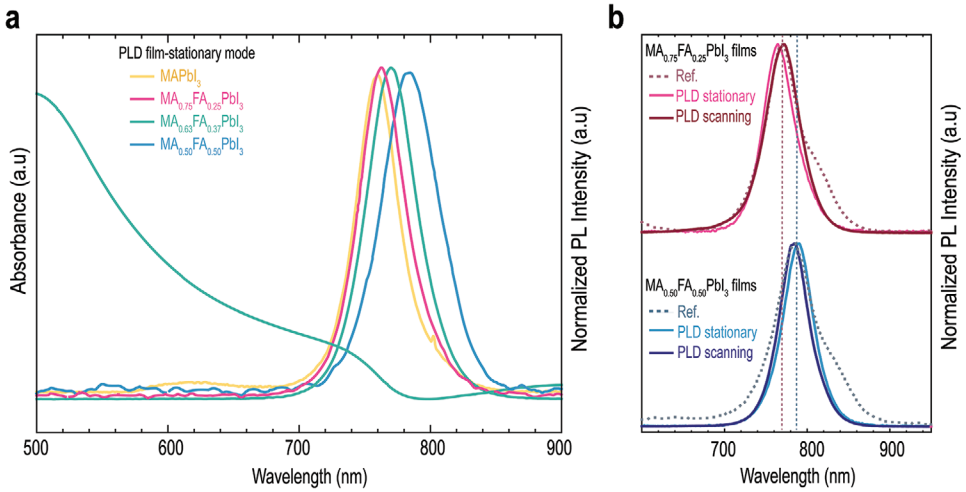

Figure 4. a) Photoluminescence spectra of $MA_{1-x}FA_xPbI_3$ (x = 0–0.50) thin films grown by PLD with the stationary mode, showing a redshift with increasing FA^+ content in the films. The absorbance plot for $MA_{0.63}FA_{0.37}PbI_3$ is shown with a solid green line. b) Photoluminescence spectra of films grown with the stationary and scanning mode and comparison with reference stoichiometric powders containing 25% and 50% FA^+. The 'shoulders' in the reference PL spectra could be related to photon reabsorption in the bulk of the pressed powder pellets.

references. Note that the 'shoulders' in the reference PL spectra could be related to photon reabsorption due to internal reflections in the bulk of the pressed powder pellets.[60]

This confirms the stoichiometric control on the films by both PLD modes discussed. The peak positions are at 1.60 eV for 25% FA^+ and 1.57 eV for 50% FA^+.[59] There is a clear trend for the optical bandgap values compared to the cation ratio estimated from the N 1s core levels analysis (Figure S7, Supporting Information) and the peak shift observed with FA^+ incorporation in the XRD data of Figures 1d and 2b.

2.3. Basic Growth Concept for $MA_{1-x}FA_xPbI_3$ Films by PLD

To compare the growth process with other PVD methods, e.g. co-evaporation, we further studied the properties of the films at different stages of growth. **Figure 5**a illustrates a simplified interpretation of the different PLD $MA_{1-x}FA_xPbI_3$ growth steps (see Figure 5c), primarily based on XRD patterns taken at different thickness stages of the films. Note that this does not consider other possible contributions from potential decomposition products of the organic molecules, surface diffusion, etc.[61–63] From XRD patterns (Figure 5c), we note that the first 20 nm of the growth indicates the formation of a PbI_2-rich layer, as seen by the prominent (002) peak of PbI_2. This is in agreement with other PVD processes suggesting that the sticking of the organic molecules starts to occur after the initial formation of a PbI_2 seed layer.[36,64–66] At a thickness of ≈100 nm, the main perovskite diffraction peaks corresponding to the $MA_{1-x}FA_xPbI_3$ (100), (111), and (200) orientations increase in intensity, and the PbI_2 diffraction peak remains constant, indicating the coexistence of the metal halide and the perovskite with probably more organohalides interdiffusion and reactions encouraging the perovskite formation. The PbI_2 peak starts decreasing with thickness until only the perovskite peaks are visible for the 500 nm thick films, suggesting full conversion to perovskite. When employing the stationary mode at these three growth stages, we notice a delay in the PbI_2 conversion, which could be related to fewer organic molecules in the center of the plasma plume (Figure S16, Supporting Information). Figure 5b displays AFM scans at the different thickness stages, showing the thin film evolution from the contact layers to an $MA_{1-x}FA_xPbI_3$ film containing a homogeneous distribution of small grains. Figure 5d,e displays the morphology of narrow columnar grains that could be promoted due to the limited coarsening of grains on a substrate kept at RT.[65] A strong link between the substrate surface energy to achieve columnar grain growth has been reported for vapor-based methods.[64]

Finally, to test if an organic-rich atmosphere forms in the chamber during PLD of the hybrid perovskites, as suggested for co-evaporation,[64] we prepared ≈100 nm PbI_2 thin films from a pure PbI_2 target and placed them next to the main process substrate (Figure S17, Supporting Information). When the shutter protected the PbI_2 thin film, no perovskite transformation was observed by XRD; however, when the shutter was left entirely open, the XRD showed the perovskite peaks corresponding to the transformation of the PbI_2 thin film. This finding suggests that there is an organic-rich environment during the growth of hybrid halide perovskite by PLD but still in a confined region near the plasma plume. This is important when performing deposition with the scanning mode, as discussed in Section 2.1.2.

2.4. PLD perovskite absorbers incorporated in solar cells

Figure 6a,d shows the performance parameters of proof-of-concept solar cells with the developed PLD-grown $MA_{0.55}FA_{0.45}PbI_3$ perovskite absorber. We performed RT depositions, and no post-treatment, such as annealing or bulk or surface passivation, to test the intrinsic quality of the as-deposited PLD-$MA_{0.55}FA_{0.45}PbI_3$ films. The device stack was glass/ITO/SnO_2/PCBM/$MA_{0.55}FA_{0.45}PbI_3$ (420 nm)/ Spiro MeOTAD/Au. Figure 6a exhibits the current-voltage (J–V) characteristics of

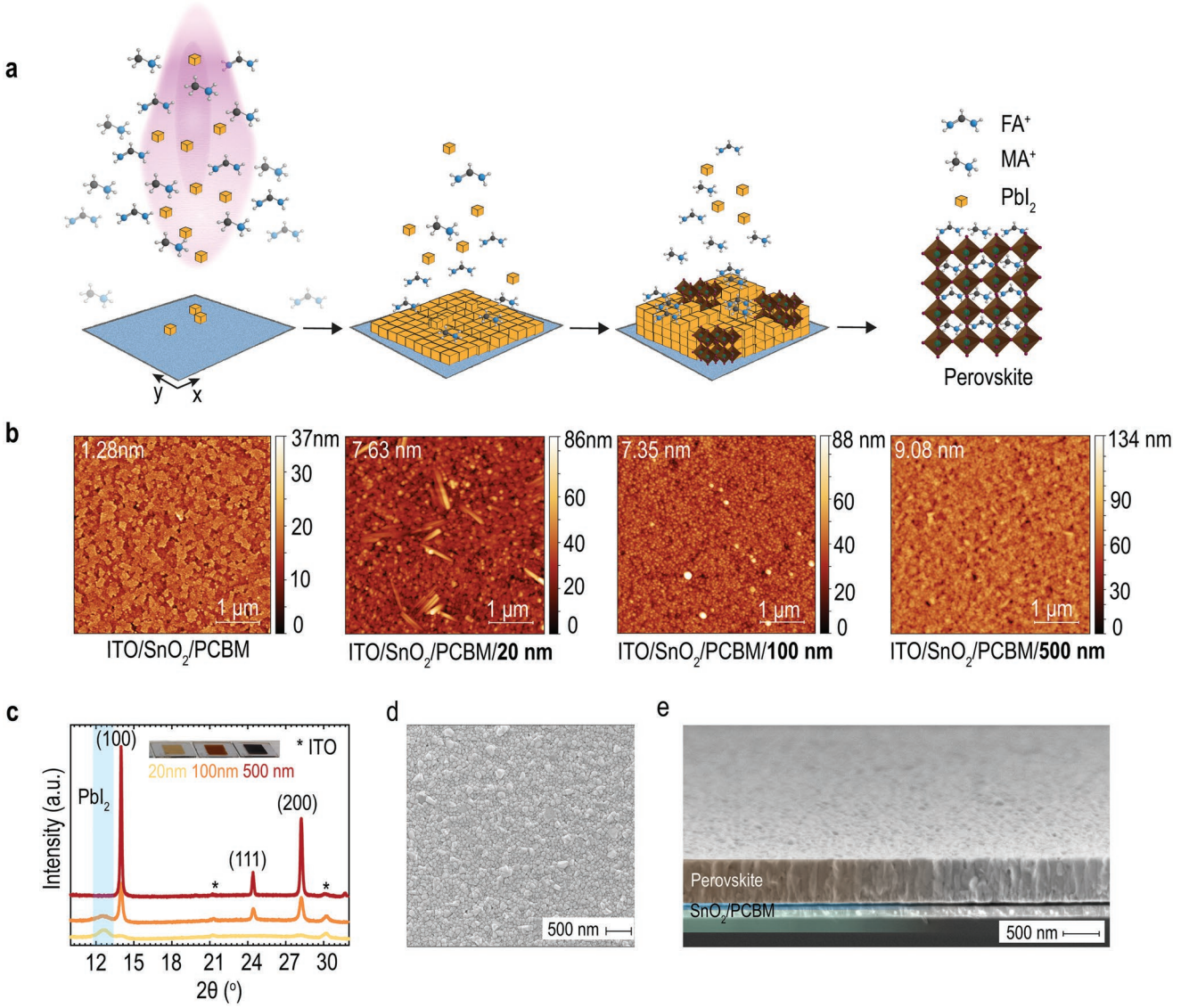

Figure 5. a) Schematic illustration of the PLD growth process of $MA_{1-x}FA_xPbI_3$ films. A PbI_2-rich layer forms during the first nanometers of the growth, implying a preferential sticking of the metal halides onto the substrates followed by the adhesion of the organic molecules involving possible interdiffusion and subsequent reactions to form the halide perovskite film. b) Atomic force microscopy images of the film at different thickness stages and comparison with the contact layers stack (ITO/SnO_2/PCBM) and final film topography (ITO/SnO_2/PCBM/ $MA_{1-x}FA_xPbI_3$–500 nm). c) XRD patterns of films at different growth stages (inset: photographs of the films). d,e): HR-SEM of a 500 nm $MA_{1-x}FA_xPbI_3$ perovskite film absorber grown on ITO/SnO_2/PCBM d) top view secondary electron image revealing a film with compact and grainy morphology with ≈100 nm average grain sizes, e) Cross section of $MA_{1-x}FA_xPbI_3$ thin film on contact layers demonstrating a homogeneous distribution of grains following a columnar growth.

the best-performing cell. The device generated a short circuit current density (J_{sc}) of almost 20 mA cm^{-2} but showed a limited open circuit voltage (V_{oc}) and fill factor (FF) of ≈1.00 V and ≈70%, respectively, thus giving a maximum PCE of ≈14%. There are several reasons for the lower device performance when compared to state-of-the-art perovskite cells. First, optimization of the halide perovskite layer thickness is required to improve the optics of the device, and therefore, J_{sc}.[67–69] Bulk and surface passivation of the perovskite is known as critical steps for improving V_{oc} and FF losses, e.g., additives such as $PbCl_2$,[10] MACl[70,71] in bulk or incorporating 2D passivation[72–75] are all important next steps for further device optimization. Another critical step is the optimization of contact layers (both ETL and HTL) to ensure efficient carrier extraction and, with it, improved FF and J_{sc}. Finally, the observed hysteresis of the devices, mainly affecting the FF as observed in Figure 6d, which could be attributed to 1. non-optimized contacts, for instance, unbalanced charge transport/extraction at the ETL and HTL, particularly when employing doped-Spiro MeOTAD[76] or, 2. the double organic cation composition as suggested by Silver–Hamill and co-authors.[77] which could be drastically reduced by incorporating other cations, such as Cs^+ and Rb^+.[78]

All-vacuum deposited n-i-p devices incorporating the optimized PLD-$MA_{0.55}FA_{0.45}PbI_3$ absorber and evaporated contacts

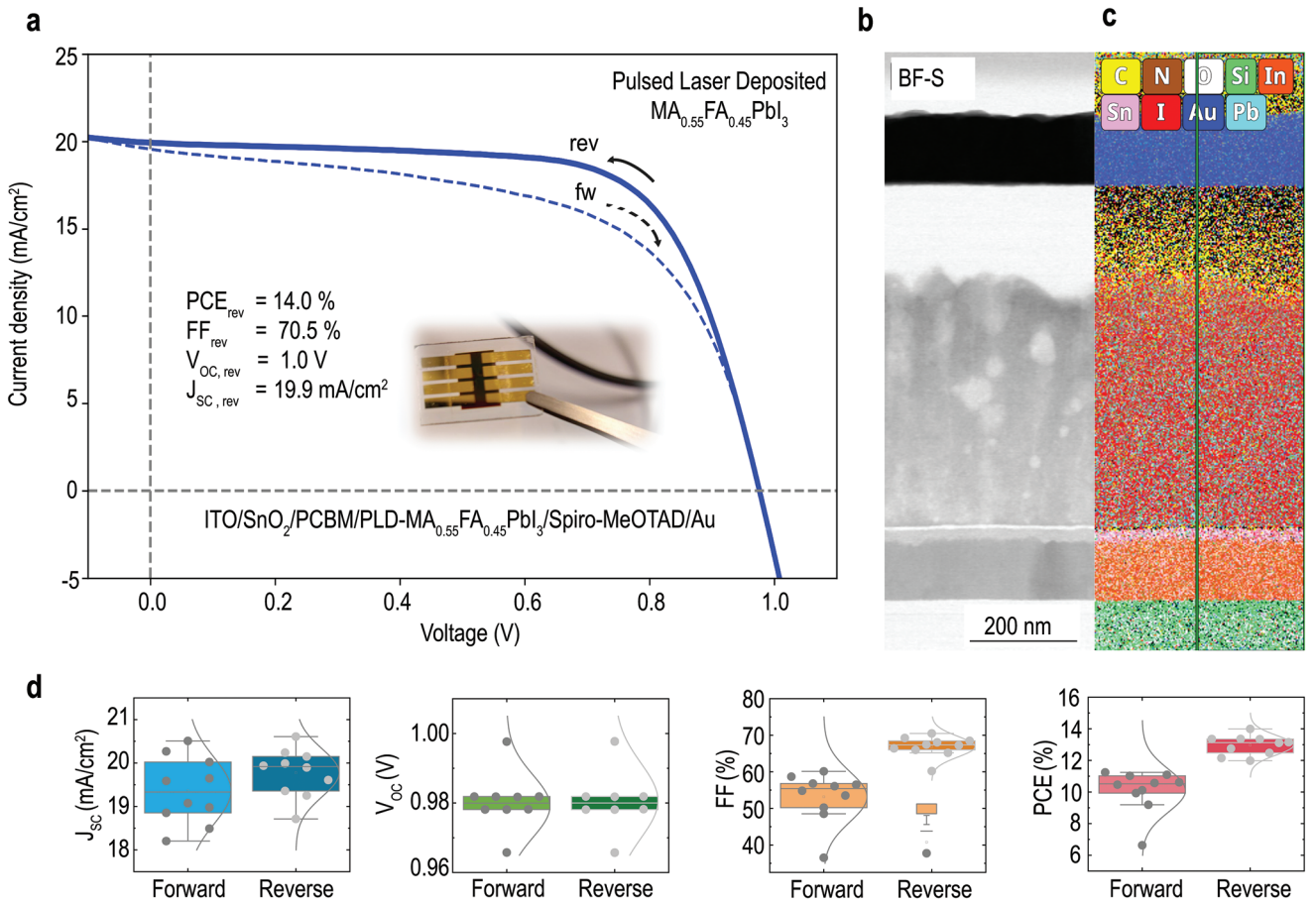

Figure 6. a) *J–V* characteristics of proof-of-concept solar cells with $MA_{0.55}FA_{0.45}PbI_3$ absorber layer (420 nm thick) deposited by the scanning PLD mode. b) Cross section Bright Field (BF) imaging of ITO/SnO_2 /PCBM/PLD-$MA_{0.55}FA_{0.45}PbI_3$/ Spiro-MeOTAD/Au showing defined interfaces and columnar grains. c) STEM EDX map indicating a homogeneous element distribution through the device stack. d) Device properties of the solar cell parameters extracted from the reverse (V_{oc}→J_{sc}) and forward (J_{sc}→V_{oc}) *J–V* scans.

(Figure S21, Supporting Information) were also tested. While the hysteresis was reduced, lower power conversion efficiencies (9.9% best pixel) were obtained, possibly also related to non-optimized perovskite thickness and because the substrates were not freshly coated.

To corroborate the solar cell stack and the microstructure of the perovskite, we performed cross-section STEM EDX maps (see Figure 6b,c) displaying defined interfaces and a homogeneous distribution of elements. Mainly the absorber layer shows a homogeneous composition through the film with columnar grain width of ≈100 nm. Some of the features in the TEM image of the perovskite are related to the FIB sample preparation. We moreover point out that the PLD-$MA_{0.55}FA_{0.45}PbI_3$ films are sufficiently stable to carry out characterization in air (e.g., PL, XRD, and AFM), and the integrated devices (also measured in air and without encapsulation) could be measured after two months of fabrication as shown in Figure S22 (Supporting Information).

Finally, while the efficiencies of these proof-of-concept devices are below state-of-the-art n-i-p cells, the potential of the PLD-$MA_{0.55}FA_{0.45}PbI_3$ absorber, deposited at room temperature, without any passivation, and from a single source is demonstrated. Various optimization pathways, as indicated above, are important next steps to enhance device efficiencies.

3. Conclusion

We reported the successful growth of $MA_{1-x}FA_xPbI_3$ films with the photoactive cubic α-phase by PLD at room temperature. This demonstrates that PLD allows the direct transfer of two distinct organic cations, i.e., MA^+ and FA^+, and the inorganic components from a single solid source. Stoichiometry control was furthermore demonstrated with stationary and scanning PLD mode, representing an important step for the future scalability of the method for large-area depositions. We furthermore discussed the critical role of the target composition and PLD parameters to achieve the desired thin film stoichiometry. Additionally, the stoichiometry and integrity of the organic molecules in the films were confirmed by XPS and solid-state NMR. The presence of extra signals in the solid-state NMR spectra suggests the need for further optimization of the film quality. Finally, proof-of-concept solar cells with room-temperature deposited $MA_{1-x}FA_xPbI_3$ films with no

further passivation nor post-treatment delivered promising conversion efficiencies of 14% for the best cell. Future applications of PLD include wide-bandgap perovskites for monolithic tandem devices, with PLD presenting the advantage of stoichiometry control from a single source, together with the intrinsic conformal coating and thickness control of vapor deposition methods.

4. Experimental Section

PLD Targets: Methylammonium iodide (MAI, > 99.99% greatcell solar), formamidinium iodide (FAI, > 99.99% greatcell solar), and lead iodide (PbI_2, 99.999% Sigma-Aldrich) powders were weighted (analytical balance, ± 0.01 mg) inside an N_2 filled glovebox. Non-stoichiometric ratios of the inorganic to the organic components (PbI_2: MAI/FAI = 1:8) were used as determined in previous optimization work.[19] The ratio of organic components MAI:FAI was varied from 100:0 to 0:100 for the different cation ratios. The powders were transferred to zirconia vials and mixed using a homemade rotatory ball milling for 48 h with zirconia balls. Subsequently, the mixed powders were uniaxially pressed at room temperature employing 470 MPa into a 2.5 mm thick disc of 20 mm in diameter. The PLD targets were pre-ablated before each deposition and polished in between depositions.

Pulsed Laser Deposition (PLD): Pulsed Laser Deposition (PLD) was performed using a Coherent KrF excimer laser (λ = 248 nm) to ablate the solid target inside a customized (TSST Demcon) vacuum chamber in an Ar atmosphere (working pressures: 0.01–0.05 mbar). Multiple depositions from a single target were performed on a "fresh" ground area of the target. A target-to-substrate distance of 55 mm was kept constant for all the depositions. All depositions were performed at RT (≈25 °C). The laser fluence varied between 0.20–0.60 J cm^{-2} during the optimization process and was kept at 0.31 mJ cm^{-2} for the optimized conditions. For all samples (unless otherwise stated), a frequency of 4 Hz, 12000 pulses (corresponding to 500 nm-thick films), and a spot size of 2.33 mm^2 were used.

X-Ray Diffraction (XRD): Measurements were done in a symmetric configuration using a PANalytical X'Pert PRO with a Cu anode X-ray source both on films and PLD targets.

Optical Properties: A Perkin Elmer Lambda 950 S UV–vis–NIR spectrophotometer with InGaAs integrating sphere was used to measure transmittance and reflectance, to extract the absorbance of the films.

Photoluminescence (PL): Measurements were done in a home-built setup consisting of a 520 nm laser Diode Module, 100 mW (Matchbox series), and a StellarNetBLUE-Wave Spectrometer coupled with a fiber optic.

X-ray Photoelectron Spectroscopy (XPS): Measurements were performed using an Omicron XM 1000 Al Kα monochromated X-ray source (1486.6 eV, FWHM = 0.26 eV) and an Omicron EA 125 energy analyzer with a pass energy of 50 eV, at a photoemission angle θ of 55° and 5°. An electron neutralizer beam is used to minimize binding energy shifts. During measurements, the pressure was < 3×10^{-10} mbar. The samples were fixed with a copper double-sided conductive adhesive tape and analyzed as loaded. The spectra' peak positions and width were fitted using a Gaussian–Lorentzian function (GL). A Shirley background was employed using the CasaXPS Software. During the fitting, constraints of the peak position and peak area were employed based on the reported data. Adventitious carbon was set at 484.85 for all samples.

MAS-ss-NMR: Magic angle spinning solid-state NMR experiments were carried out on a Bruker AVANCE IIIHD spectrometer, B_0 = 22.3 T (ν_0 = 950.13 MHz for ^{1}H) using a 1.3 mm HXY MAS probe employing spinning speeds between 20 and 40 kHz. ^{1}H chemical shifts were referenced using a solid sample of adamantane (1H δiso = 1.85 ppm). Six thin films were scraped from the substrate (≈50 mg of the sample), packed into rotors in air, and processed immediately. ^{1}H DEPTH was employed to suppress the signals coming from the polymers present in the cap of the rotors.

Atomic Force Microscopy (AFM): Images were taken using a Bruker Icon Dimension in Tapping mode in air.

TEM Lamella: The lamella was cut at 30 kV and subsequently thinned at 5, 2, and 1 kV employing a Thermo Fisher Helios 5 Dual Beam FIB

STEM Imaging: STEM Imaging was taken employing The Spectro 300 S/TEM (Thermo Fisher Scientific) using a high-angle angular dark-field detector combined with EDX spectroscopy at an acceleration voltage of 300 kV.

Secondary Electron SEM Images: Secondary Electron SEM Images were acquired with acceleration voltages ranging from 0.75 to 1.5 kV using a Zeiss MERLIN HR-SEM.

Device Preparation: ITO glass substrates (20 × 15 mm, Ossila) were cleaned in ultrasonic baths of 2 v/v % solution of Hellmanex III, deionized water, acetone, and 2-propanol for 10 min each, followed by a 20 min Oxygen plasma treatment. As an electron transport layer, 20 nm SnO_2 nanoparticles were coated using a dynamically double-step spin coating at 3500 rpm for 60 s and annealed at 150 °C for 10 and 30 min, respectively. Afterward, oxygen plasma treatment was performed for 10 min. Subsequently, a solution of (6,6)-Phenyl C61 butyric acid methyl ester (PCBM, 160848-22-6 Lumtec; 3 mg mL^{-1}) was prepared in anhydrous chlorobenzene (108-90-7, Sigma Aldrich) and spin-coated onto the SnO_2 in one step at 5000 rpm for 60 s. The freshly coated contacts were transferred to the PLD chamber directly from the glovebox (without exposure to air) for the perovskite absorber deposition. A background pressure of ≤ 7×10^{-7} mbar was utilized in the PLD for all batches of samples. A customized PLD target was pre-ablated for 460 pulses at 4 Hz using a working pressure between 0.025–0.033 mbar and a laser fluence of 0.31 mJ cm^{-2} using a 248 nm UV laser. To deposit 450 nm thick film, 12000 and 13500 pulses were employed for the stationary and scanning mode (30 × 30 mm^2), respectively. All depositions were performed at RT (25 °C). Next, the samples were transferred through the load lock into the glove box. As a hole transport layer, 200 nm doped Spiro-MeOTAD (50 mg, 207739-72-8, Sigma Aldrich) in 498 uL of anhydrous chlorobenzene (108-90-7, Sigma Aldrich) was coated onto the as-deposited PLD-grown absorbers at 3000 rpm for 30 s. Spiro-MeOTAD additives are LiTFSI (10 µL, 90076-65-6, Sigma Aldrich) from a stock solution of 520 mg mL^{-1} in extra dry acetonitrile (75-05-8, Sigma Aldrich) and 3-tert-Bytylpyridine (18 µL, TBP, 397881–2, Sigma Aldrich). Finally, 90 nm of Au was sputtered using RF sputtering in 2 steps (step one: control voltage –200 V, Ar flow: 99 mL min^{-1}, 0.08 mbar, t = 12.5 min; step two: control forward power 50 W, Ar flow: 20 mL min^{-1}, 0.02 mbar, t = 15 min).

Device Characterization: The *J–V* characteristics of the devices were recorded using an Ossila Source-Measure Unit and LED solar simulator SINUS-70 (Wavelabs) under a controlled ambient atmosphere (30–35% humidity). *J–V* curves were measured under simulated AM 1.5G illumination in both forward ($J_{sc}\rightarrow V_{oc}$) and reverse ($V_{oc}\rightarrow J_{sc}$) directions with a scan rate of 110 mVs^{-1} employing a 1 mm^2 illumination mask. The intensity was calibrated with monocrystalline silicon WPV *N*-type broadband reference solar cell to match the global standard AM 1.5 G spectrum with an intensity of 100 mW cm^{-2}.

Supporting Information

Supporting Information is available from the Wiley Online Library or from the author.

Acknowledgements

This project was financed by the European Research Council (ERC) under the European Union's Horizon 2020 Research and Innovation Program (CREATE, Grant Agreement No. 852722). The authors would like to thank D.M Cunha, Y. Smirnov, Y. A. Birkhölzer, P-A Repecaud, M. Huijben, G. Rijnders, and G. Koster for fruitful discussions; N. Rodkey, A. Peñaherrera, and TSST Demcon for their experimental

support; D. Post for his technical assistance; M. Smithers, M. Goodwin, and M. Tsvetanova for SEM and STEM imaging. K.P.S.Z acknowledges support from the Spanish Ministry of Science and Innovation via a Juan de la Cierva scholarship (IJC2020-045130-I). A.P. acknowledges a Grisolia scholarship from Generalitat Valenciana (GRISOLIAP/2020/134). J. S. G. and A. P. N. K. thank the Dutch Research Council (NWO) for the support of the "Solid-State NMR Facility for Advanced Materials Science," which is part of the uNMR-NL ROADMAP facility (grant nr. 184.035.002). The NMR facilities technicians Gerrit Janssen, Hans Janssen, and Ruud Aspers are thanked for their support.

Conflict of Interest

The authors declare no conflict of interest.

Data Availability Statement

The data that support the findings of this study are available from the corresponding author upon reasonable request.

Keywords

mixed-organic-cation halide perovskites, physical vapor deposition, pulsed laser deposition, solvent-free methods, stoichiometry control, vacuum-processed perovskite solar cells

Received: January 31, 2023
Published online: March 16, 2023

[1] J. Jean, P. R. Brown, *Emerging Photovoltaic Technologies*, IOP Publishing, Bristol, UK **2020**.
[2] M. Roß, S. Severin, M. B. Stutz, P. Wagner, H. Köbler, M. Favin-Lévêque, A. Al-Ashouri, P. Korb, P. Tockhorn, A. Abate, B. Stannowski, B. Rech, S. Albrecht, *Adv. Energy Mater.* **2021**, *11*, 2101460.
[3] F. Sahli, J. Werner, B. A. Kamino, M. Bräuninger, R. Monnard, B. Paviet-Salomon, L. Barraud, L. Ding, J. J. Diaz Leon, D. Sacchetto, G. Cattaneo, M. Despeisse, M. Boccard, S. Nicolay, Q. Jeangros, B. Niesen, C. Ballif, *Nat. Mater.* **2018**, *17*, 820.
[4] J. Ávila, C. Momblona, P. P. Boix, M. Sessolo, H. J. Bolink, *Joule* **2017**, *1*, 431.
[5] J. Li, H. Wang, X. Y. Chin, H. A. Dewi, K. Vergeer, T. W. Goh, J. W. M. Lim, J. H. Lew, K. P. Loh, C. Soci, T. C. Sum, H. J. Bolink, N. Mathews, S. Mhaisalkar, A. Bruno, *Joule* **2020**, *4*, 1035.
[6] L. Gil-Escrig, C. Momblona, M. G. La-Placa, P. P. Boix, M. Sessolo, H. J. Bolink, *Adv. Energy Mater.* **2018**, *8*, 1703506.
[7] Y. H. Chiang, M. Anaya, S. D. Stranks, *ACS Energy Lett.* **2020**, *5*, 2498.
[8] L. Gil-Escrig, C. Dreessen, F. Palazon, Z. Hawash, E. Moons, S. Albrecht, M. Sessolo, H. J. Bolink, *ACS Energy Lett.* **2021**, *6*, 827.
[9] G. Longo, C. Momblona, M. G. La-Placa, L. Gil-Escrig, M. Sessolo, H. J. Bolink, *ACS Energy Lett.* **2018**, *3*, 214.
[10] K. B. Lohmann, S. G. Motti, R. D. J. Oliver, A. J. Ramadan, H. C. Sansom, Q. Yuan, K. A. Elmestekawy, J. B. Patel, J. M. Ball, L. M. Herz, H. J. Snaith, M. B. Johnston, *ACS Energy Lett.* **2022**, *7*, 1903.
[11] M. M. Byranvand, C. Otero-Martínez, J. Ye, W. Zuo, L. Manna, M. Saliba, R. L. Z. Hoye, L. Polavarapu, *Adv. Opt. Mater.* **2022**, *10*, 2200423.
[12] K. Drużbicki, R. Lavén, J. Armstrong, L. Malavasi, F. Fernandez-Alonso, M. Karlsson, *J. Phys. Chem. Lett.* **2021**, *12*, 3503.
[13] N. Pellet, P. Gao, G. Gregori, T. Y. Yang, M. K. Nazeeruddin, J. Maier, M. Grätzel, *Angew. Chem. Int. Ed.* **2014**, *53*, 3151.
[14] Y. Zhang, G. Grancini, Y. Feng, A. M. Asiri, M. K. Nazeeruddin, *ACS Energy Lett.* **2017**, *2*, 802.
[15] L. Gil-Escrig, C. Dreessen, I. C. Kaya, B. Kim, F. Palazon, M. Sessolo, H. Bolink, *ACS Energy Lett.* **2020**, *5*, 3053.
[16] V. M. Kiyek, Y. A. Birkhölzer, Y. Smirnov, M. Ledinsky, Z. Remes, J. Momand, B. J. Kooi, G. Koster, G. Rijnders, M. Morales-Masis, *Adv. Mater. Interfaces* **2020**, *7*, 2000162.
[17] H. Wang, Y. Wu, M. Ma, S. Dong, Q. Li, J. Du, H. Zhang, Q. Xu, *ACS Appl. Energy Mater.* **2019**, *2*, 2305.
[18] N. Rodkey, S. Kaal, P. Sebastia-Luna, Y. A. Birkhölzer, M. Ledinsky, F. Palazon, H. J. Bolink, M. Morales-Masis, *Chem. Mater.* **2021**, *33*, 7417.
[19] T. Soto-Montero, W. Soltanpoor, S. Kralj, Y. A. Birkhölzer, Z. Remes, G. Rijnders, M. Morales-masis, *IEEE 48th Photovolt. Spec. Conf.*, IEEE, Piscataway, NJ **2021**.
[20] U. Bansode, S. Ogale, *J. Appl. Phys.* **2017**, *121*, 133107.
[21] W. A. Dunlap-Shohl, E. T. Barraza, A. Barrette, K. Gundogdu, A. D. Stiff-Roberts, D. B. Mitzi, *ACS Energy Lett.* **2018**, *3*, 270.
[22] U. Bansode, R. Naphade, O. Game, S. Agarkar, S. Ogale, *J. Phys. Chem. C* **2015**, *119*, 9177.
[23] R. Vidal, J. A. Alberola-Borràs, S. N. Habisreutinger, J. L. Gimeno-Molina, D. T. Moore, T. H. Schloemer, I. Mora-Seró, J. J. Berry, J. M. Luther, *Nat. Sustain.* **2021**, *4*, 277.
[24] Z. Hong, D. Tan, R. A. John, Y. K. E. Tay, Y. K. T. Ho, X. Zhao, T. C. Sum, N. Mathews, F. García, H. Sen Soo, *iScience* **2019**, *16*, 312.
[25] F. Palazon, Y. El Ajjouri, H. J. Bolink, *Adv. Energy Mater.* **2020**, *10*, 1902499.
[26] Y. Smirnov, L. Schmengler, R. Kuik, P. A. Repecaud, M. Najafi, D. Zhang, M. Theelen, E. Aydin, S. Veenstra, S. De Wolf, M. Morales-Masis, *Adv. Mater. Technol.* **2021**, *6*, 2000856.
[27] D. H. A. Blank, M. Dekkers, G. Rijnders, *J. Phys. D. Appl. Phys.* **2014**, *47*, 034006.
[28] R. Eason, *Pulsed Laser Deposition of Thin Films*, (Ed.: R. Eason), John Wiley & Sons, Inc., Hoboken, New Jersey **2007**.
[29] A. Ojeda-G-P, M. Döbeli, T. Lippert, *Adv. Mater. Interfaces* **2018**, *5*, 1701062.
[30] H. Gruninger, M. Bokdam, N. Leupold, P. Tinnemans, R. Moos, G. A. De Wijs, F. Panzer, A. P. M. Kentgens, *J. Phys. Chem. C* **2021**, *125*, 1742.
[31] D. J. Kubicki, D. Prochowicz, A. Hofstetter, P. Péchy, S. M. Zakeeruddin, M. Grätzel, L. Emsley, *J. Am. Chem. Soc.* **2017**, *139*, 10055.
[32] W. Li, M. U. Rothmann, Y. Zhu, W. Chen, C. Yang, Y. Yuan, Y. Y. Choo, X. Wen, Y. B. Cheng, U. Bach, J. Etheridge, *Nat. Energy* **2021**, *6*, 624.
[33] A. Maqsood, Y. Li, J. Meng, D. Song, B. Qiao, S. Zhao, Z. Xu, *Nanoscale Res. Lett.* **2020**, *15*, 89.
[34] T. J. Jacobsson, J. P. Correa-Baena, E. Halvani Anaraki, B. Philippe, S. D. Stranks, M. E. F. Bouduban, W. Tress, K. Schenk, J. Teuscher, J. E. Moser, H. Rensmo, A. Hagfeldt, *J. Am. Chem. Soc.* **2016**, *138*, 10331.
[35] B. wook Park, N. Kedem, M. Kulbak, D. Y. Lee, W. S. Yang, N. J. Jeon, J. Seo, G. Kim, K. J. Kim, T. J. Shin, G. Hodes, D. Cahen, S. Il Seok, *Nat. Commun.* **2018**, *9*, 1.
[36] B. S. Kim, L. Gil-Escrig, M. Sessolo, H. J. Bolink, *J. Phys. Chem. Lett.* **2020**, *11*, 6852.
[37] K. P. S. Zanoni, A. Paliwal, M. A. Hernández-Fenollosa, P. A. Repecaud, M. Morales-Masis, H. J. Bolink, *Adv. Mater. Technol.* **2022**, *7*, 2101747.
[38] Y. Smirnov, P. A. Repecaud, L. Tutsch, I. Florea, K. P. S. Zanoni, A. Paliwal, H. J. Bolink, P. R. Cabarrocas, M. Bivour, M. Morales-Masis, *Mater. Adv.* **2022**, *3*, 3469.

[39] B. Philippe, G. J. Man, H. Rensmo, in *Characterization Techniques for Perovskite Solar Cell Materials*, (Eds.: M. Pazoki, A. Hagfeldt, T. Edvinsson), Elsevier, New York **2019**.
[40] S. Béchu, M. Ralaiarisoa, A. Etcheberry, P. Schulz, *Adv. Energy Mater.* **2020**, *10*, 1.
[41] J. Rodriguez-Pereira, J. Tirado, A. F. Gualdrón-Reyes, F. Jaramillo, R. Ospina, *Surf. Sci. Spectra* **2020**, *27*, 024003.
[42] R. L. Z. Hoye, P. Schulz, L. T. Schelhas, A. M. Holder, K. H. Stone, J. D. Perkins, D. Vigil-Fowler, S. Siol, D. O. Scanlon, A. Zakutayev, A. Walsh, I. C. Smith, B. C. Melot, R. C. Kurchin, Y. Wang, J. Shi, F. C. Marques, J. J. Berry, W. Tumas, S. Lany, V. Stevanović, M. F. Toney, T. Buonassisi, *Chem. Mater.* **2017**, *29*, 1964.
[43] C. Das, M. Wussler, T. Hellmann, T. Mayer, W. Jaegermann, *Phys. Chem. Chem. Phys.* **2018**, *20*, 17180.
[44] N. Fairley, V. Fernandez, M. Richard-Plouet, C. Guillot-Deudon, J. Walton, E. Smith, D. Flahaut, M. Greiner, M. Biesinger, S. Tougaard, D. Morgan, J. Baltrusaitis, *Appl. Surf. Sci. Adv.* **2021**, *5*, 100112.
[45] I. S. Zhidkov, D. W. Boukhvalov, A. F. Akbulatov, L. A. Frolova, L. D. Finkelstein, A. I. Kukharenko, S. O. Cholakh, C. C. Chueh, P. A. Troshin, E. Z. Kurmaev, *Nano Energy* **2021**, *79*, 105421.
[46] J. F. Moulder, W. F. Stickle, P. E. Sobol, K. D. Bomben, *Handbook of X-ray Photoelectron Spectroscopy*, Perkin-Elmer Corporation, Eden Prairie, Minnesota **1995**.
[47] S. Olthof, K. Meerholz, *Sci. Rep.* **2017**, *7*, 40267.
[48] D. J. Kubicki, S. D. Stranks, C. P. Grey, L. Emsley, *Nat. Rev. Chem.* **2021**, *5*, 624.
[49] B. Reif, S. E. Ashbrook, L. Emsley, M. Hong, *Nat. Rev. Methods Prim.* **2021**, *1*, 2.
[50] W. M. J. Franssen, A. P. M. Kentgens, *Solid State Nucl. Magn. Reson.* **2019**, *100*, 36.
[51] C. Pareja-Rivera, A. L. Solís-Cambero, M. Sánchez-Torres, E. Lima, D. Solis-Ibarra, *ACS Energy Lett.* **2018**, *3*, 2366.
[52] W. M. J. Franssen, B. J. Bruijnaers, V. H. L. Portengen, A. P. M. Kentgens, *ChemPhysChem* **2018**, *19*, 3107.
[53] A. Pisanu, C. Ferrara, P. Quadrelli, G. Guizzetti, M. Patrini, C. Milanese, C. Tealdi, L. Malavasi, *J. Phys. Chem. C* **2017**, *121*, 8746.
[54] W. T. M. Van Gompel, R. Herckens, G. Reekmans, B. Ruttens, J. D'Haen, P. Adriaensens, L. Lutsen, D. Vanderzande, *J. Phys. Chem. C* **2018**, *122*, 4117.
[55] C. J. Dahlman, D. J. Kubicki, G. N. M. Reddy, *J. Mater. Chem. A* **2021**, *9*, 19206.
[56] D. J. Kubicki, D. Prochowicz, A. Hofstetter, S. M. Zakeeruddin, M. Grätzel, L. Emsley, *J. Am. Chem. Soc.* **2017**, *139*, 14173.
[57] N. Landi, E. Maurina, D. Marongiu, A. Simbula, S. Borsacchi, L. Calucci, M. Saba, E. Carignani, M. Geppi, *J. Phys. Chem. Lett.* **2022**, *13*, 9517.
[58] F. Aiello, S. Masi, *Nanomaterials* **2021**, *11*, 2024.
[59] A. Francisco-López, B. Charles, M. I. Alonso, M. Garriga, M. Campoy-Quiles, M. T. Weller, A. R. Goñi, *J. Phys. Chem. C* **2020**, *124*, 3448.
[60] K. Schötz, A. M. Askar, W. Peng, D. Seeberger, T. P. Gujar, M. Thelakkat, A. Köhler, S. Huettner, O. M. Bakr, K. Shankar, F. Panzer, *J. Mater. Chem. C* **2020**, *8*, 2289.
[61] J. Borchert, I. Levchuk, L. C. Snoek, M. U. Rothmann, R. Haver, H. J. Snaith, C. J. Brabec, L. M. Herz, M. B. Johnston, *ACS Appl. Mater. Interfaces* **2019**, *11*, 28851.
[62] M. J. Bækbo, O. Hansen, I. Chorkendorff, P. C. K. Vesborg, *RSC Adv.* **2018**, *8*, 29899.
[63] M. Roß, M. B. Stutz, S. Albrecht, *Sol. RRL* **2022**, *6*, 2200500.
[64] T. Abzieher, T. Feeney, F. Schackmar, Y. J. Donie, I. M. Hossain, J. A. Schwenzer, T. Hellmann, T. Mayer, M. Powalla, U. W. Paetzold, *Adv. Funct. Mater.* **2021**, *31*, 2104482.
[65] Q. Guesnay, F. Sahli, C. Ballif, Q. Jeangros, *APL Mater.* **2021**, *9*, 100703.
[66] K. B. Lohmann, J. B. Patel, M. U. Rothmann, C. Q. Xia, R. D. J. Oliver, L. M. Herz, H. J. Snaith, M. B. Johnston, *ACS Energy Lett.* **2020**, *5*, 710.
[67] M. Koç, W. Soltanpoor, G. Bektaş, H. J. Bolink, S. Yerci, *Adv. Opt. Mater.* **2019**, *7*, 1900944.
[68] F. Mathies, H. Eggers, B. S. Richards, G. Hernandez-Sosa, U. Lemmer, U. W. Paetzold, *ACS Appl. Energy Mater.* **2018**, *1*, 1834.
[69] M. Rai, L. H. Wong, L. Etgar, *J.Phys. Chem. Lett* **2020**, *11*, 8189.
[70] A. Z. Chen, B. J. Foley, J. H. Ma, M. R. Alpert, J. S. Niezgoda, J. J. Choi, *J. Mater. Chem. A* **2017**, *5*, 7796.
[71] Q. Dong, Y. Yuan, Y. Shao, Y. Fang, Q. Wang, J. Huang, *Energy Enviromental Sci.* **2015**, *8*, 2464.
[72] R. Azmi, E. Ugur, A. Seitkhan, F. Aljamaan, A. S. Subbiah, J. Liu, G. T. Harrison, M. I. Nugraha, M. K. Eswaran, M. Babics, Y. Chen, F. Xu, T. G. Allen, A. ur Rehman, C. L. Wang, T. D. Anthopoulos, U. Schwingenschlögl, M. De Bastiani, E. Aydin, S. De Wolf, *Science* **2022**, *376*, 73.
[73] Y. W. Jang, S. Lee, K. M. Yeom, K. Jeong, K. Choi, M. Choi, J. H. Noh, *Nat. Energy* **2021**, *6*, 63.
[74] K. T. Cho, G. Grancini, Y. Lee, E. Oveisi, J. Ryu, O. Almora, M. Tschumi, P. A. Schouwink, G. Seo, S. Heo, J. Park, J. Jang, S. Paek, G. Garcia-Belmonte, M. K. Nazeeruddin, *Energy Environ. Sci.* **2018**, *11*, 952.
[75] H. S. Yoo, N. G. Park, *Sol. Energy Mater. Sol. Cells* **2018**, *179*, 57.
[76] J. Ren, Z. Kan, *Origin of Hysteresis in Perovskite Solar Cells*, Vol. *060903*, AIP Publishing LLC, Melville, New York **2020**.
[77] S. H. Turren-Cruz, M. Saliba, M. T. Mayer, H. Juárez-Santiesteban, X. Mathew, L. Nienhaus, W. Tress, M. P. Erodici, M. J. Sher, M. G. Bawendi, M. Grätzel, A. Abate, A. Hagfeldt, J. P. Correa-Baena, *Energy Environ. Sci.* **2018**, *11*, 78.
[78] Y. Hu, E. M. Hutter, P. Rieder, I. Grill, J. Hanisch, M. F. Aygüler, A. G. Hufnagel, M. Handloser, T. Bein, A. Hartschuh, K. Tvingstedt, V. Dyakonov, A. Baumann, T. J. Savenije, M. L. Petrus, P. Docampo, *Adv. Energy Mater.* **2018**, *1703057*, 1.